

Effect of GRB spectra on the empirical luminosity correlations and the GRB Hubble diagram

Hai-Nan Lin^{1*}, Xin Li^{1,2†}, Zhe Chang^{3‡}

¹*Department of Physics, Chongqing University, Chongqing 401331, China*

²*State Key Laboratory of Theoretical Physics, Institute of Theoretical Physics, Chinese Academy of Sciences, Beijing 100190, China*

³*Institute of High Energy Physics, Chinese Academy of Sciences, Beijing 100049, China*

Accepted xxxx; Received xxxx; in original form xxxx

ABSTRACT

The spectra of gamma-ray bursts (GRBs) in a wide energy range can usually be well described by the Band function, which is a two smoothly jointed power laws cutting at a breaking energy. Below the breaking energy, the Band function reduces to a cut-off power law, while above the breaking energy it is a simple power law. However, for some detectors (such as the Swift-BAT) whose working energy is well below or just near the breaking energy, the observed spectra can be fitted to cut-off power law with enough precision. Besides, since the energy band of Swift-BAT is very narrow, the spectra of most GRBs can be fitted well even using a simple power law. In this paper, with the most up-to-date sample of Swift-BAT GRBs, we study the effect of different spectral models on the empirical luminosity correlations, and further investigate the effect on the reconstruction of GRB Hubble diagram. We mainly focus on two luminosity correlations, i.e., the Amati relation and Yonetoku relation. We calculate these two luminosity correlations on both the case that the GRB spectra are modeled by Band function and cut-off power law. It is found that both luminosity correlations only moderately depend on the choice of GRB spectra. Monte Carlo simulations show that Amati relation is insensitive to the high-energy power-law index of the Band function. As a result, the GRB Hubble diagram calibrated using luminosity correlations is almost independent on the GRB spectra.

Key words: cosmological parameters – gamma-ray burst: general

1 INTRODUCTION

Gamma-ray bursts (GRBs), mainly emitting radiation in the gamma-ray waveband which lasts a few seconds, and may be followed by the X-ray, optical or radio emissions lasting a few days, are the most energetic explosions in the Universe (Piran 1999; Mészáros 2006; Kumar & Zhang 2015). The recent decades have seen great successes in understanding the nature of GRBs thanks to the contribution by various space experiments. The isotropic distribution in the sky strongly implies that GRBs happen in the deep universe (Paciesas et al. 1999). The cosmological origin of GRBs was eventually confirmed starting from 1997 thanks to the combination of accurate localizations by BeppoSAX and redshift measurements from the follow-up observation with the main optical/IR facilities. The furthest GRB observed at

present has redshift ~ 9.4 (Cucchiara et al. 2011), and the total isotropic equivalent radiated energy by a GRB is about $10^{48} \sim 10^{55}$ ergs (Kumar & Zhang 2015). The durations of GRBs span about six orders of magnitude, from milliseconds for the shortest to thousands of seconds for the longest. It is widely accepted that GRBs can be divided into two classes according to the duration, because the histogram of duration is fitted well by the summation of two Gauss functions separated at around 2 seconds (Kouveliotou et al. 1993). Therefore, short and long GRBs are classified depending on whether the duration is shorter or longer than 2 seconds. The light curves of GRBs have various type, from smoothly decaying to highly variable with many spikes (Fishman & Meegan 1995). The spectrum of a typical GRB can be well fitted by the Band function (Band et al. 1993), which is a two smoothly jointed power laws cutting at a breaking energy. Below the breaking energy, the Band function reduces to the cut-off power law (CPL), and above the breaking energy, it is the simple power law (PL). However, some detectors such as the Swift-BAT, work in an energy band well below or just

* e-mail: linhainan@jyzjcn@163.com.

† e-mail: lixin1981@cqu.edu.cn.

‡ e-mail: changz@ihep.ac.cn.

near the breaking energy. Therefore, it is enough to fit the spectra just with the simple PL, and the high-energy power-law index of the Band function couldn't be constrained.

Since the first linear correlation between the spectral lag and the isotropic peak luminosity ($\tau_{\text{lag}} - L$ relation) was found by Norris, Marani & Bonnell (2000), several other empirical correlations have been found. These empirical correlations relate the luminosity to the spectral parameters of GRBs. One of the most famous correlation was found by Amati et al. (2002). The Amati relation is a linear (in the logarithmic scale) correlation between the isotropic equivalent energy and the peak energy of νF_ν spectra ($E_p - E_{\text{iso}}$ relation). Later, Yonetoku et al. (2004) found a similar correlation between the isotropic peak luminosity and the peak energy ($E_p - L$ relation). Other two-parameter luminosity correlations includes: $V - L$ relation (Fenimore & Ramirez-Ruiz 2000), $E_p - E_\gamma$ relation (Ghirlanda, Ghisellini & Lazzati 2004), $\tau_{\text{RT}} - L$ relation (Schaefer 2007), and so on. Besides, there are also three-parameter correlations such as $E_{\text{iso}} - E_p - t_b$ relation (Liang & Zhang 2005), $L - E_p - T_{0.45}$ relation (Firmani et al. 2006), $E_{X,\text{iso}} - E_{\gamma,\text{iso}} - E_p$ relation (Bernardini et al. 2012; Margutti et al. 2013), $L - E_p - \Gamma_0$ relation (Liang et al. 2015). Some luminosity correlations are only valid for long GRBs, while others are valid for both short and long GRBs. These correlations are often used to calibrate GRBs as the standard candles and to reconstruct the GRB Hubble diagram (Schaefer 2003; Dai, Liang & Xu 2004; Ghirlanda et al. 2004; Liang & Zhang 2005; Firmani et al. 2005; Schaefer 2007; Amati 2008; Basilakos & Perivolaropoulos 2008; Liang et al. 2008; Liang & Zhang 2008; Wei & Zhang 2009; Wei 2010; Liu & Wei 2014; Wang et al. 2015; Lin, Li & Chang 2015).

The above luminosity correlations involve three quantities, i.e., the isotropic equivalent energy E_{iso} , the isotropic peak luminosity L and the spectral peak energy E_p . The derivation of the first two quantities involves the integration of spectra over the “bolometric” 1 – 10000 keV energy band. However, most detectors such as Swift-BAT only measure photons in a narrow energy band. Therefore, we should extrapolate the observed spectra to the whole energy band. Most previous works calculated E_{iso} and L by assuming that the spectra are modeled by the Band function. Due to the narrow energy width of detectors, CPL (or even PL) is enough to fit the observed spectra, and the high-energy index (β) of the Band function can't be constrained. Schaefer (2007) fixed β to be -2.2 for all the GRBs that have no measured β . In fact, about 60% (41 out of 69) GRBs compiled in Schaefer (2007) have no measurement of β . The following works (Liang et al. 2008; Basilakos & Perivolaropoulos 2008; Xiao & Schaefer 2009; Wei 2010; Wang, Qi & Dai 2011; Liu & Wei 2014) which cited the data from Schaefer (2007) also have the underlying assumption that the unmeasured β 's are all set to be -2.2 . It is especially necessary to check such a setting has some influence on the final luminosity correlations. Using 29 Swift GRBs, Cabrera et al. (2007) found that the zero-point of Amati relation calculated from CPL is slightly larger than that from Band function, while the intercept does not change significantly. The small change of zero-point of Amati relation may have some influences on the calibration of GRBs.

In this paper, we investigate if the luminosity correlations are affected by the choice of GRB spectra. We search

the most up-to-date Swift data archive¹ and find that among ~ 300 GRBs which have redshift measurement, only 44 GRBs can be well fitted by CPL so have well defined peak energy. Using the 44 GRBs, we study the $E_p - E_{\text{iso}}$ correlation and $E_p - L$ correlation. All the 44 GRBs are fitted by CPL so the high-energy index couldn't be determined. Therefore, we calculate E_{iso} and L by using the CPL instead of the Band function. To comparison, we also calculate E_{iso} and L using the Band function, with the high-energy index fixed to be -2.2 , the median value of BATSE GRBs (Preece et al. 2000), as was done by Schaefer (2007). We further calibrate the distance of GRBs using these two luminosity correlations respectively, and reconstruct GRB Hubble diagram. We investigate the influence of different spectra on the luminosity correlations and on the reconstruction of GRB Hubble diagram. Throughout this paper, we assume the concordance cosmological model with the fiducial parameters $H_0 = 70 \text{ km s}^{-1} \text{ Mpc}^{-1}$, $\Omega_M = 0.28$ and $\Omega_\Lambda = 0.72$.

The rest of this paper is arranged as follows: In Section 2, we present the observational properties of 44 Swift-BAT GRBs used in our analysis. In Section 3, we investigate the $E_p - E_{\text{iso}}$ relation and $E_p - L$ relation by assuming that the GRB spectrum is modeled by Band function and CPL, respectively, and compare their differences. We also implement Monte Carlo simulations to test the sensitivity of luminosity correlations on the high-energy power-law index. In Section 4, we calibrate the distance of GRBs through these two luminosity correlations, to see whether the resulting GRB Hubble diagram would depend on the choice of spectra. Finally, Section 5 is devoted to a short summary.

2 THE OBSERVATIONAL PROPERTIES OF SWIFT GRBS

The Swift satellite, launched on November 20, 2004, is a first-of-its-kind multi-wavelength observatory dedicated to the study of GRB science. There are three instruments onboard Swift working together to observe GRBs and afterglows in the gamma-ray, X-ray, ultraviolet, and optical wavebands. The Burst Alert Telescope (BAT, 15 – 150 keV), which is a highly sensitive and large field of view gamma-ray detector working in the energy band 15 – 150 keV, detects GRBs and accurately determines their positions on the sky. Soon after the triggering of BAT, the X-ray Telescope (XRT, 0.3 – 10 keV) and UV/Optical Telescope (UVOT, 170 – 600 nm) quickly repoint the field of view towards GRBs and start the afterglow observation. With the rate of about 100 GRBs per year, Swift has observed about one thousand GRBs until September, 2015, and about 300 GRBs have redshift measurement.

For most GRBs, the spectra can be well fitted by a two smoothly jointed power laws cutting at a breaking energy E_b , which is well known as the Band function (Band et al.

¹ <http://swift.gsfc.nasa.gov/>.

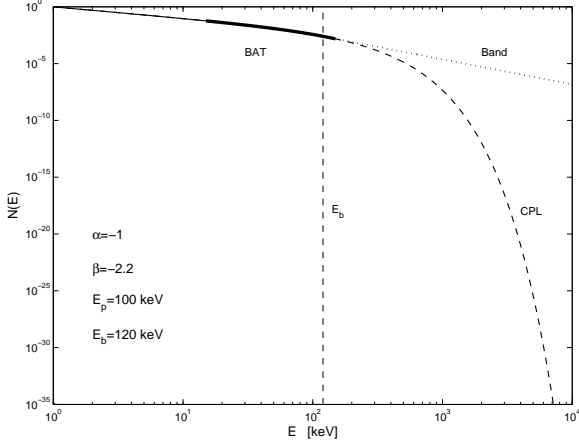


Figure 1. The difference between Band function and CPL. The vertical axis is normalized so that $N(E = 1 \text{ keV}) = 1$. The dashed curve is the CPL, and the dotted curve is the Band function. The vertical dashed line represents the breaking energy $E_b \equiv [(\alpha - \beta)/(2 + \alpha)]E_p$. The black solid curve represents the energy band (15 – 150 keV) in which the Swift-BAT is sensitive. The parameters in this figure are: $\alpha = -1$, $\beta = -2.2$, $E_p = 100 \text{ keV}$, and $E_b = 120 \text{ keV}$.

1993),

$$N_{\text{Band}}(E) = \begin{cases} AE^\alpha \exp\left[-(2 + \alpha)\frac{E}{E_p}\right] & E \leq \frac{\alpha - \beta}{2 + \alpha}E_p, \\ BE^\beta & E > \frac{\alpha - \beta}{2 + \alpha}E_p, \end{cases} \quad (1)$$

where α and β are the low-energy and high-energy power-law index, respectively, and they vary from bursts to bursts. Statistically, α peaks around -1 , and β peaks around -2.2 (Preece et al. 2000). The Band function is continuous and smooth at the breaking energy $E_b \equiv (\alpha - \beta)/(2 + \alpha)E_p$, and it is monotonously decreasing in the whole energy range. However, it is easy to prove that the $\nu F_\nu \propto E^2 N(E)$ spectrum has a peak at $E = E_p$, for any $\alpha \geq -2$ and $\beta < -2$. The distribution of E_p depends on the specific detectors. For the BATSE catalog, E_p peaks around 150 keV (Preece et al. 2000), while for the Swift-BAT catalog, E_p is relatively lower (Sakamoto et al. 2011). The Band function was first proposed from analyzing the spectra of GRBs observed by BATSE, which is a gamma-ray detector sensitive in a wide energy band 20 – 2000 keV. However, the Swift-BAT is only sensitive in a low and narrow energy band, which is just near or even below the typical breaking energy. Therefore, the observed spectra by Swift-BAT can be fitted using the low-energy end of Band function, i.e., the CPL,

$$N_{\text{CPL}}(E) = AE^\alpha \exp\left[-(2 + \alpha)\frac{E}{E_p}\right]. \quad (2)$$

This is to say, the high-energy index β can't be well constrained. The CPL is a special case of Band function in the limit $\beta \rightarrow \infty$. Figure 1 shows the difference between the Band function and CPL. CPL falls much more dramatically than Band function above E_b . On the other hand, since the Swift-BAT working energy band is very narrow, for majority of GRBs we can even fit the spectra just with a simple

PL, i.e.,

$$N_{\text{PL}}(E) = AE^\alpha. \quad (3)$$

The νF_ν spectrum of CPL also peaks at E_p , while PL is monotonous and has no peak.

Among ~ 300 Swift GRBs with measured redshift, only 44 GRBs have a reasonable CPL fit so have well determined peak energy, while the remaining GRBs can be fitted well by the simple PL. Only these 44 GRBs are available to analyze the luminosity correlations. We list the observational properties of the 44 GRBs in Table 1. The errors in this table are of 90% confidence level (C.L.). All of the 44 GRBs are long GRBs with duration $T_{90} > 2$ seconds². The observed photon fluence spans three orders of magnitude, while the peak photon flux spans two orders of magnitude. Figure 2(a) is the histogram of redshift of the 44 GRBs. The redshift of our sample ranges from 0.347 to 9.4, with a median value 1.9. Figure 2(b) is the histogram of the low-energy power-law index. A Gauss fit to the histogram gives the average value $\bar{\alpha} = -1.05 \pm 0.14$ and standard deviation $\sigma_\alpha = 0.38 \pm 0.14$ (95% C.L.). Two GRBs (GRB 131117A and GRB 130612A) have positive index. Figure 2(c) is the distribution of the observed peak energy E_p , ranging from 19.2 keV to 258 keV, with a median value 71.4 keV. Only 9% (4 out of 44) GRBs have peak energy above the BAT energy range. All the remaining GRBs have peak energy well within the BAT energy range. This is one reason why the high-energy power-law index can't be well constrained. In Figure 2(d) we plot the histogram of the rest frame peak energy $E_{p,i} = E_p \times (1 + z)$, which ranges from 38 keV to 693 keV. The distribution of $E_{p,i}$ is more homogeneous compared to that of E_p .

3 THE LUMINOSITY CORRELATIONS

The most investigated GRB luminosity correlations are those between the total radiated energy or luminosity (calculated in a fixed energy band) and the spectral peak energy. Here we focus on discussing two luminosity correlations, i.e., the Amati relation ($E_p - E_{\text{iso}}$) and Yonetoku relation ($E_p - L$).

The Amati relation is a linear (in the logarithmic scale) correlation between isotropic equivalent energy and peak energy of νF_ν spectrum in the comoving frame (Amati et al. 2002; Amati 2003, 2006). It was first discovered by Amati et al. (2002) in 12 long BeppoSAX GRBs and was confirmed in larger samples (Amati 2003, 2006). Later it was found that short GRBs do not follow the same Amati relation of long GRBs (Amati, Frontera & Guidorzi 2009; Amati 2010). The physical origin of Amati relation has been discussed but selection effect couldn't be excluded. Amati relation is one of the most used relations in calibrating the distance of GRBs, although there are still some controversies on its validity (Li

² The duration of a GRB usually characterized by T_{90} , in which time from 5% to 95% photons are recorded. The duration of GRB 130925A is not measured, but it is very likely to be a long GRB, because all the other GRBs having reliable CPL fit are long GRBs, and GRB 130925A follows the Amati relation and Yonetoku relation of the remaining GRBs (see section 3).

Table 1. The observed properties of 44 Swift-BAT GRBs. Column (1): the GRB identifier. Columns (2) and (3): the Right Ascension and Declination (J2000) in unit of degree. Column (4): the GRB duration in which time 90% photons are recorded. Column (5): the redshift. Column (6): the observed photon fluence in 15 – 150 keV energy band in unit of 10^{-7} erg cm $^{-2}$. Column (7): the observed peak photon flux in 15 – 150 keV energy band in unit of photons cm $^{-2}$ s $^{-1}$. Column (8): the photon index. Column (9): the observed peak energy in unit of keV. Column (10): the GCN Circular numbers (http://gcn.gsfc.nasa.gov/gcn3_archive.html). All the errors in this table are of 90% C.L. Note that in the Swift data archive, the uncertainties of E_p (and/or S , P , α) of some GRBs are not symmetric. We symmetrize them by taking the average, i.e., $\sigma = (\sigma_- + \sigma_+)/2$.

(1) GRBs	(2) RA	(3) DEC	(4) T_{90}	(5) z	(6) S	(7) P	(8) α	(9) E_p	(10) GCN Circ.
141220A	195.058	+32.146	7.21	1.3195	26 ± 1	8.9 ± 0.7	-0.62 ± 0.38	117.4 ± 45.1	17196; 17202
140518A	227.231	+42.396	60.5	4.707	10 ± 1	1.0 ± 0.1	-0.92 ± 0.61	43.9 ± 7.6	16298; 16306
140515A	186.071	+15.099	23.4	6.32	5.9 ± 0.6	0.9 ± 0.1	-0.98 ± 0.64	51.3 ± 14.7	16267; 16284
140206A	145.321	+66.762	93.6	2.73	160 ± 3	19.4 ± 0.5	-1.04 ± 0.15	100.9 ± 14.5	15784; 15805
131117A	332.354	-31.761	11	4.18	2.5 ± 0.4	0.7 ± 0.1	$+0.40 \pm 1.41$	44.0 ± 7.4	15490; 15499; 15500
130925A	41.186	-26.146	...	0.347	410 ± 10	7.3 ± 0.6	-1.85 ± 0.14	33.4 ± 20.0	15246; 15257
130701A	357.224	+36.100	4.38	1.155	44 ± 1	17.1 ± 0.7	-0.90 ± 0.21	89.2 ± 12.4	14953; 14959
130612A	259.771	+16.729	4	2.006	2.3 ± 0.5	1.7 ± 0.3	$+0.14 \pm 1.71$	36.4 ± 7.6	14874; 14916
130420A	196.118	+59.421	123.5	1.297	71 ± 3	3.4 ± 0.2	-1.52 ± 0.25	33.2 ± 6.8	14406; 14419
120923A	303.781	+6.255	27.2	8.5	3.2 ± 0.8	0.6 ± 0.1	-0.29 ± 1.66	44.4 ± 10.6	13796; 13807
120922A	234.758	-20.181	173	3.1	62 ± 7	2.0 ± 0.2	-1.58 ± 0.36	38.2 ± 0.0	13793; 13806
120811C	199.690	+62.297	26.8	2.671	30 ± 3	4.1 ± 0.2	-1.40 ± 0.30	42.9 ± 5.7	13622; 13634
120802A	44.833	+13.762	50	3.796	19 ± 3	3.0 ± 0.2	-1.21 ± 0.47	57.2 ± 19.4	13555; 13559
120724A	245.193	+3.535	72.8	1.48	6.8 ± 1.1	0.6 ± 0.2	-0.53 ± 1.53	27.6 ± 7.5	13510; 13517
120326A	273.906	+69.248	69.6	1.798	26 ± 3	4.6 ± 0.2	-1.41 ± 0.34	41.1 ± 6.9	13105; 13120
110726A	286.713	+56.070	5.2	1.036	2.2 ± 0.3	1.0 ± 0.2	-0.64 ± 0.87	46.5 ± 11.8	12196; 12201
110715A	237.665	-46.237	13	0.82	118 ± 2	53.9 ± 1.1	-1.25 ± 0.12	120 ± 21	12158; 12160
110503A	132.799	+52.211	10	1.613	100 ± 4	1.35 ± 0.06	-0.88 ± 0.25	133 ± 54	11991; 11995
110422A	112.057	+75.100	25.9	1.77	410 ± 10	30.7 ± 1.0	-0.86 ± 0.10	149.4 ± 18.5	11957; 11959
100816A	351.738	+26.568	2.9	0.8034	20 ± 1	10.9 ± 0.4	-0.73 ± 0.24	170.7 ± 79.7	11102; 11111; 11113
091029	60.166	-55.954	39.2	2.752	24 ± 1	1.8 ± 0.1	-1.46 ± 0.27	61.4 ± 17.5	10097; 10103
091018	32.191	-57.546	4.4	0.971	14 ± 1	10.3 ± 0.4	-1.77 ± 0.24	19.2 ± 14.5	10034; 10040
090926B	46.310	-38.997	109.7	1.24	73 ± 2	3.2 ± 0.3	-0.52 ± 0.24	78.3 ± 7.0	9935; 9939
090618	294.008	+78.352	113.2	0.54	1050 ± 10	38.9 ± 0.8	-1.42 ± 0.08	134 ± 19	9512; 9530; 9534
090429B	210.672	+32.167	5.5	9.4	3.1 ± 0.3	1.6 ± 0.2	-0.47 ± 0.77	42.1 ± 5.6	9281; 9290
090424	189.531	+16.829	48	0.544	210 ± 0	71 ± 2	-1.19 ± 0.15	108.6 ± 20.3	9223; 9231
090423	148.891	+18.165	10.3	8	5.9 ± 0.4	1.7 ± 0.2	-0.80 ± 0.50	48.6 ± 6.2	9198; 9204; 9241
081222	22.748	-34.095	24	2.77	48 ± 1	7.7 ± 0.2	-1.08 ± 0.15	131 ± 31	8691; 8709
081221	15.801	-24.542	34	2.26	181 ± 3	18.2 ± 0.5	-1.21 ± 0.13	69.9 ± 3.9	8687; 8708
081121	89.282	-60.612	14	2.512	41 ± 3	4.4 ± 1.0	-0.43 ± 0.54	123 ± 69	8537; 8539
080916A	336.289	-57.026	60	0.689	40 ± 1	2.7 ± 0.2	-1.17 ± 0.21	94.6 ± 23.0	8237; 8243
080913	65.741	-25.127	8	6.44	5.6 ± 0.6	1.4 ± 0.2	-0.46 ± 0.70	93.1 ± 56.1	8217; 8222
080605	262.130	+4.010	20	1.6398	133 ± 2	19.9 ± 0.6	-1.11 ± 0.14	223 ± 133	7828; 7839; 7841
080603B	176.554	+68.061	60	2.69	24 ± 1	3.5 ± 0.2	-1.21 ± 0.30	71 ± 16	7794; 7806
080413B	326.138	-19.981	8	1.1	32 ± 1	18.7 ± 0.8	-1.26 ± 0.27	73.3 ± 15.8	7598; 7606; 7610
080207	207.514	+7.492	340	2.0858	61 ± 2	1.0 ± 0.3	-1.17 ± 0.27	107.8 ± 72.5	7264; 7272; 7277
071010B	150.531	+45.733	35.7	0.947	44 ± 1	7.7 ± 0.3	-1.53 ± 0.22	52.0 ± 6.4	6871; 6877
070521	242.659	+30.260	37.9	0.553	80.10 ± 1.77	6.53 ± 0.27	-1.10 ± 0.17	195 ± 123	6431; 6440
070508	312.832	-78.382	20.9	0.82	196.00 ± 2.73	24.10 ± 0.61	-1.14 ± 0.12	258 ± 134	6383; 6390
060927	329.547	+5.370	22.5	5.6	11.30 ± 0.68	2.70 ± 0.17	-0.93 ± 0.38	71.7 ± 17.6	5627; 5639
060707	357.069	-17.904	66.2	3.43	16.00 ± 1.51	1.01 ± 0.23	-0.66 ± 0.63	66.0 ± 17.5	5285; 5289
060206	202.933	+35.046	7.6	4.045	8.31 ± 0.42	2.79 ± 0.17	-1.06 ± 0.34	75.4 ± 19.5	4682; 4697
060115	54.007	+17.339	139.6	3.53	17.1 ± 1.5	0.87 ± 0.12	-1.00 ± 0.50	62.0 ± 20.5	4509; 4518
050525A	278.142	+26.335	8.8	0.606	153.00 ± 2.21	41.70 ± 0.94	-1.00 ± 0.10	79 ± 4	3466; 3467; 3479

2007; Dainotti et al. 2013; Lin et al. 2015). We can parameterize Amati relation as

$$\log \frac{E_{\text{iso}}}{\text{erg}} = a + b \log \frac{E_{p,i}}{300 \text{ keV}}, \quad (4)$$

where $E_{p,i} = E_p \times (1+z)$ is the peak energy in the rest frame, and

$$E_{\text{iso}} = 4\pi d_L^2 S_{\text{bolo}} (1+z)^{-1} \quad (5)$$

is the isotropic equivalent energy in the rest frame 1–10,000

keV energy band, and d_L is the luminosity distance. In the concordance cosmological model, the luminosity distance is given by

$$d_L(z) = (1+z) \frac{c}{H_0} \int_0^z \frac{dz}{\sqrt{\Omega_M(1+z)^3 + (1-\Omega_M)}}. \quad (6)$$

The bolometric fluence S_{bolo} is calculated from the observed photon fluence S and GRB spectra $N(E)$ in the rest frame

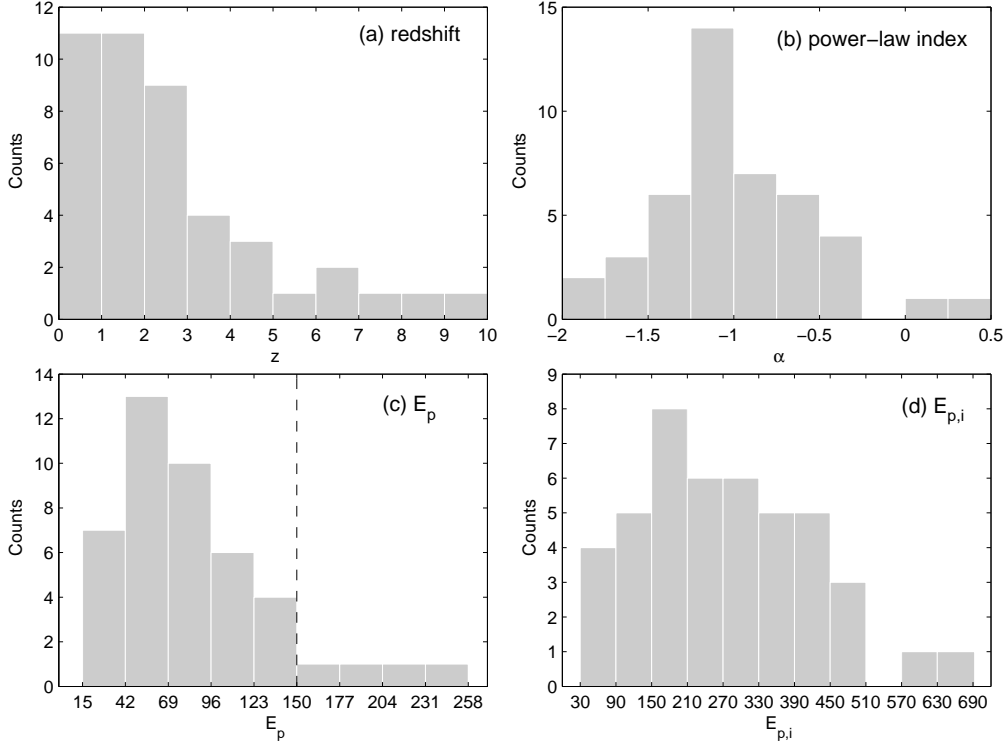


Figure 2. The histograms of (a) the redshift z , (b) the power-law index α , (c) the observed peak energy E_p , and (d) the rest-frame peak energy $E_{p,i}$. The vertical dashed line in panel (c) is the upper boundary of the BAT energy band.

1 – 10,000 keV energy band (Schaefer 2007),

$$S_{\text{bolo}} = S \times \frac{\int_{1/(1+z)}^{10^4/(1+z)} EN(E)dE}{\int_{E_{\min}}^{E_{\max}} EN(E)dE}, \quad (7)$$

where $E_{\min} = 15$ keV and $E_{\max} = 150$ keV are the lower and upper boundary of the BAT energy band, respectively. The bolometric fluence S_{bolo} , as well as the isotropic equivalent energy E_{iso} , depend on the GRB spectra. We calculate S_{bolo} and E_{iso} in both cases that GRB spectra are modeled by Band function and CPL. Since the high-energy power-law index of the Band function can't be measured, we fix it to be -2.2 , the peak of BATSE catalog (Preece et al. 2000). The final results are listed in columns (2) – (5) in Table 2. Errors are given in 1σ C.L. We only consider the error propagation from S . As is expected, the isotropic equivalent energy calculated from Band function is much larger than that from CPL, since CPL falls much faster than Band function above the breaking energy.

The Yonetoku relation is first found by Yonetoku et al. (2004) from the combination of 12 BeppoSAX GRBs and 11 BATSE GRBs. It is similar to the Amati relation except that the isotropic equivalent energy E_{iso} is replaced by the isotropic peak luminosity L , i.e.,

$$\log \frac{L}{\text{erg s}^{-1}} = a + b \log \frac{E_{p,i}}{300 \text{ keV}}. \quad (8)$$

The isotropic peak luminosity L can be calculated from the bolometric peak flux P_{bolo} as

$$L = 4\pi d_L^2 P_{\text{bolo}}, \quad (9)$$

while the bolometric peak flux P_{bolo} is calculated from the

observed peak photon flux P in the rest frame 1 – 10,000 keV energy band by integrating over the GRB spectra (Schaefer 2007),

$$P_{\text{bolo}} = P \times \frac{\int_{1/(1+z)}^{10^4/(1+z)} EN(E)dE}{\int_{E_{\min}}^{E_{\max}} N(E)dE}. \quad (10)$$

We also calculate P_{bolo} and L in both the Band and CPL spectra cases, and list the results in columns (2) – (5) in Table 3. Errors are given in 1σ C.L. The errors of P_{bolo} and L are propagated from the errors of P . Similarly, we can see that the peak luminosity calculated from Band function is much larger than that from CPL.

In order to see more clearly the effect of GRB spectra on the final isotropic energy (and peak luminosity), we calculate the difference of isotropic energy (and peak luminosity) derived from Band and CPL spectra,

$$\begin{cases} \Delta E_{\text{iso}} \equiv \frac{E_{\text{iso}}^{\text{Band}} - E_{\text{iso}}^{\text{CPL}}}{E_{\text{iso}}^{\text{CPL}}}, \\ \Delta L \equiv \frac{L^{\text{Band}} - L^{\text{CPL}}}{L^{\text{CPL}}}. \end{cases} \quad (11)$$

We plot ΔE_{iso} and ΔL versus the power-law index α in Figure 3. We can see that both ΔE_{iso} and ΔL are positively correlated with α . When α is close to -2 , both ΔE_{iso} and ΔL are small. This is because the difference between Band function and CPL model becomes smaller when α approaches β .

Both Amati relation and Yonetoku relation have the

Table 2. The bolometric fluence, isotropic equivalent energy, and distance modulus calibrated using the Amati relation. Column (1): the GRB identifier. Columns (2) and (3): the bolometric fluence in unit of 10^{-7} erg/cm². Columns (4) and (5): the isotropic equivalent energy in unit of 10^{52} ergs. Columns (6) and (7): the distance modulus calibrated using the Amati relation. The superscripts “CPL” and “Band” mean that the quantities are calculated using the CPL and Band function, respectively. All the errors in this table are of 1σ C.L.

(1) GRBs	(2) $S_{\text{bolo}}^{\text{CPL}}$	(3) $S_{\text{bolo}}^{\text{Band}}$	(4) $E_{\text{iso}}^{\text{CPL}}$	(5) $E_{\text{iso}}^{\text{Band}}$	(6) μ^{CPL}	(7) μ^{Band}
141220A	39.83 ± 0.93	70.20 ± 1.65	1.83 ± 0.04	3.24 ± 0.08	46.023 ± 1.245	45.864 ± 1.200
140518A	14.29 ± 0.87	21.08 ± 1.29	5.93 ± 0.36	8.74 ± 0.53	48.019 ± 1.225	48.053 ± 1.179
140515A	8.43 ± 0.52	12.16 ± 0.75	5.42 ± 0.34	7.85 ± 0.49	49.316 ± 1.236	49.381 ± 1.190
140206A	254.35 ± 2.91	385.53 ± 4.41	43.78 ± 0.50	66.34 ± 0.76	44.883 ± 1.223	44.899 ± 1.176
131117A	2.85 ± 0.28	4.86 ± 0.47	1.00 ± 0.10	1.68 ± 0.16	49.541 ± 1.229	49.433 ± 1.183
130925A	987.08 ± 14.68	1279.91 ± 19.04	3.00 ± 0.04	3.89 ± 0.06	39.950 ± 1.389	40.075 ± 1.343
130701A	64.35 ± 0.89	109.31 ± 1.51	2.29 ± 0.03	3.89 ± 0.05	45.034 ± 1.227	44.908 ± 1.180
130612A	2.84 ± 0.38	4.75 ± 0.63	0.28 ± 0.04	0.48 ± 0.06	48.175 ± 1.266	48.034 ± 1.218
130420A	139.49 ± 3.59	192.50 ± 4.96	6.22 ± 0.16	8.59 ± 0.22	43.239 ± 1.284	43.312 ± 1.235
120923A	3.95 ± 0.60	5.88 ± 0.90	3.85 ± 0.59	5.80 ± 0.88	50.561 ± 1.243	50.584 ± 1.196
120922A	127.40 ± 8.77	166.51 ± 11.46	27.13 ± 1.87	35.46 ± 2.44	44.765 ± 1.233	44.916 ± 1.185
120811C	53.33 ± 3.25	74.43 ± 4.54	8.84 ± 0.54	12.34 ± 0.75	45.597 ± 1.235	45.677 ± 1.188
120802A	29.81 ± 2.87	43.13 ± 4.15	8.82 ± 0.85	12.77 ± 1.23	47.134 ± 1.243	47.191 ± 1.198
120724A	10.47 ± 1.03	15.23 ± 1.50	0.60 ± 0.06	0.87 ± 0.09	46.011 ± 1.303	46.026 ± 1.255
120326A	46.43 ± 3.27	66.04 ± 4.65	3.82 ± 0.27	5.44 ± 0.38	45.104 ± 1.254	45.155 ± 1.206
110726A	10.76 ± 0.24	4.97 ± 0.41	0.08 ± 0.01	0.14 ± 0.01	47.554 ± 1.274	47.397 ± 1.226
110715A	213.84 ± 2.21	322.87 ± 3.34	3.85 ± 0.04	5.81 ± 0.06	43.689 ± 1.226	43.694 ± 1.179
110503A	170.72 ± 4.16	273.55 ± 6.67	11.51 ± 0.28	18.44 ± 0.45	44.842 ± 1.249	44.794 ± 1.204
110422A	743.18 ± 11.05	1169.78 ± 17.40	59.50 ± 0.88	93.65 ± 1.39	43.501 ± 1.223	43.479 ± 1.176
100816A	38.98 ± 1.19	65.91 ± 2.01	0.67 ± 0.02	1.14 ± 0.03	45.907 ± 1.258	45.799 ± 1.214
091029	43.84 ± 1.11	60.14 ± 1.53	7.64 ± 0.19	10.49 ± 0.27	46.255 ± 1.235	46.364 ± 1.189
091018	35.10 ± 1.53	44.45 ± 1.94	0.89 ± 0.04	1.12 ± 0.05	43.794 ± 1.443	43.940 ± 1.399
090926B	94.19 ± 1.57	174.84 ± 2.92	3.85 ± 0.06	7.15 ± 0.12	44.562 ± 1.228	44.336 ± 1.180
090618	2122.01 ± 12.32	3024.54 ± 17.56	16.19 ± 0.09	23.07 ± 0.13	40.953 ± 1.225	41.019 ± 1.178
090429B	4.00 ± 0.24	5.71 ± 0.34	4.54 ± 0.27	6.48 ± 0.38	50.673 ± 1.227	50.757 ± 1.180
090424	358.90 ± 0.00	568.15 ± 0.00	2.78 ± 0.00	4.40 ± 0.00	42.655 ± 1.234	42.601 ± 1.187
090423	8.00 ± 0.33	11.50 ± 0.48	7.25 ± 0.30	10.42 ± 0.43	49.762 ± 1.225	49.839 ± 1.178
081222	85.28 ± 1.08	123.41 ± 1.57	15.04 ± 0.19	21.77 ± 0.28	46.382 ± 1.235	46.456 ± 1.189
081221	285.91 ± 2.89	430.14 ± 4.35	35.50 ± 0.36	53.41 ± 0.54	44.054 ± 1.220	44.063 ± 1.173
081121	62.92 ± 2.81	108.59 ± 4.84	9.39 ± 0.42	16.21 ± 0.72	46.488 ± 1.280	46.366 ± 1.238
080916A	65.19 ± 0.99	104.26 ± 1.59	0.82 ± 0.01	1.32 ± 0.02	44.551 ± 1.241	44.485 ± 1.194
080913	7.53 ± 0.49	11.88 ± 0.78	4.98 ± 0.33	7.88 ± 0.51	50.135 ± 1.307	50.120 ± 1.264
080605	313.06 ± 2.87	438.19 ± 4.02	21.77 ± 0.20	30.46 ± 0.28	44.778 ± 1.296	44.893 ± 1.254
080603B	38.02 ± 0.97	56.41 ± 1.43	6.38 ± 0.16	9.47 ± 0.24	46.534 ± 1.227	46.562 ± 1.181
080413B	51.85 ± 0.99	80.08 ± 1.53	1.68 ± 0.03	2.59 ± 0.05	44.996 ± 1.240	44.965 ± 1.193
080207	103.81 ± 2.08	153.66 ± 3.07	11.18 ± 0.22	16.55 ± 0.33	45.514 ± 1.300	45.551 ± 1.260
071010B	82.49 ± 1.14	117.70 ± 1.63	1.98 ± 0.03	2.83 ± 0.04	43.944 ± 1.257	43.989 ± 1.209
070521	173.90 ± 2.34	266.09 ± 3.59	1.39 ± 0.02	2.13 ± 0.03	44.104 ± 1.290	44.103 ± 1.249
070508	503.41 ± 4.28	720.52 ± 6.12	9.06 ± 0.08	12.96 ± 0.11	43.608 ± 1.273	43.692 ± 1.230
060927	15.99 ± 0.59	23.77 ± 0.87	8.64 ± 0.32	12.83 ± 0.47	48.760 ± 1.236	48.804 ± 1.189
060707	20.73 ± 1.19	34.40 ± 1.98	5.21 ± 0.30	8.65 ± 0.50	47.514 ± 1.232	47.422 ± 1.186
060206	12.42 ± 0.38	18.49 ± 0.57	4.06 ± 0.13	6.06 ± 0.19	48.503 ± 1.232	48.537 ± 1.186
060115	24.48 ± 1.31	37.63 ± 2.01	6.46 ± 0.34	9.91 ± 0.53	47.310 ± 1.239	47.304 ± 1.194
050525A	224.12 ± 1.97	383.56 ± 3.38	2.17 ± 0.02	3.71 ± 0.03	42.900 ± 1.241	42.753 ± 1.193

linear form

$$y = a + bx. \quad (12)$$

The best-fitting parameters (a, b) can be derived using the likelihood method presented in D’Agostini (2005), i.e., by maximizing the following likelihood:

$$\mathcal{L}(\sigma_{\text{int}}, a, b) \propto \prod_i \frac{1}{\sqrt{\sigma_{\text{int}}^2 + \sigma_{y_i}^2 + b^2 \sigma_{x_i}^2}} \times \exp \left[-\frac{(y_i - a - bx_i)^2}{2(\sigma_{\text{int}}^2 + \sigma_{y_i}^2 + b^2 \sigma_{x_i}^2)} \right], \quad (13)$$

where σ_{int} is the intrinsic scatter, which represents the unknown errors. The introduction of intrinsic scatter is necessary since it dominates over the measurement error.

We plot the Amati relation and Yonetoku relation in Figure 4, and list the best-fitting parameters in Table 4. From Table 4, we can see that the intercept parameters of both $E_p - E_{\text{iso}}$ relation and $E_p - L$ relation calculated from the Band spectrum are moderately larger than that from CPL spectrum, while the slope parameters show no significant difference. This is consistent with the results of Cabrera

Table 3. The bolometric peak flux, isotropic peak luminosity, and distance modulus calibrated using the Yonetoku relation. Column (1): the GRB identifier. Columns (2) and (3): the bolometric peak flux in unit of 10^{-7} erg/cm²/s. Columns (4) and (5): the isotropic peak luminosity in unit of 10^{51} erg/s. Columns (6) and (7): the distance modulus calibrated using the Yonetoku relation. The superscripts “CPL” and “Band” mean that the quantities are calculated using the CPL and Band function, respectively. All the errors in this table are of 1σ C.L.

(1) GRBs	(2) $P_{\text{bolo}}^{\text{CPL}}$	(3) $P_{\text{bolo}}^{\text{Band}}$	(4) L^{CPL}	(5) L^{Band}	(6) μ^{CPL}	(7) μ^{Band}
141220A	11.39 ± 0.55	20.08 ± 0.96	12.18 ± 0.58	21.47 ± 1.03	45.297 ± 1.249	45.172 ± 1.214
140518A	0.85 ± 0.05	1.34 ± 0.08	20.02 ± 1.22	31.76 ± 1.94	47.971 ± 1.193	47.960 ± 1.156
140515A	0.80 ± 0.05	1.21 ± 0.08	37.96 ± 2.57	57.26 ± 3.88	48.751 ± 1.220	48.796 ± 1.184
140206A	22.93 ± 0.36	34.78 ± 0.55	147.17 ± 2.31	223.21 ± 3.51	45.117 ± 1.187	45.156 ± 1.150
131117A	0.47 ± 0.04	0.93 ± 0.08	8.38 ± 0.73	16.64 ± 1.45	48.442 ± 1.195	48.187 ± 1.159
130925A	10.49 ± 0.53	13.67 ± 0.69	0.43 ± 0.02	0.56 ± 0.03	42.162 ± 1.448	42.359 ± 1.412
130701A	18.53 ± 0.46	31.58 ± 0.79	14.22 ± 0.35	24.24 ± 0.61	44.145 ± 1.192	44.055 ± 1.155
130612A	1.11 ± 0.12	2.24 ± 0.24	3.34 ± 0.36	6.77 ± 0.73	46.195 ± 1.235	45.917 ± 1.198
130420A	3.78 ± 0.14	5.51 ± 0.20	3.88 ± 0.14	5.65 ± 0.20	44.214 ± 1.257	44.293 ± 1.219
120923A	0.44 ± 0.04	0.73 ± 0.07	40.96 ± 4.16	68.35 ± 6.94	49.621 ± 1.212	49.556 ± 1.176
120922A	2.41 ± 0.15	3.25 ± 0.20	21.08 ± 1.29	28.40 ± 1.73	45.991 ± 1.191	46.156 ± 1.153
120811C	4.34 ± 0.13	6.28 ± 0.19	26.41 ± 0.79	38.25 ± 1.14	45.364 ± 1.198	45.451 ± 1.161
120802A	3.01 ± 0.12	4.45 ± 0.18	42.77 ± 1.74	63.22 ± 2.57	46.755 ± 1.233	46.821 ± 1.198
120724A	0.44 ± 0.09	0.80 ± 0.16	0.63 ± 0.13	1.14 ± 0.23	46.356 ± 1.300	46.197 ± 1.262
120326A	4.84 ± 0.13	7.18 ± 0.19	11.17 ± 0.30	16.54 ± 0.44	44.682 ± 1.220	44.743 ± 1.182
110726A	0.79 ± 0.10	1.48 ± 0.18	0.46 ± 0.06	0.87 ± 0.11	46.304 ± 1.257	46.108 ± 1.220
110715A	71.55 ± 0.89	108.02 ± 1.34	23.43 ± 0.29	35.37 ± 0.44	42.907 ± 1.194	42.949 ± 1.157
110503A	1.87 ± 0.05	3.00 ± 0.08	3.29 ± 0.09	5.28 ± 0.14	47.696 ± 1.257	47.675 ± 1.222
110422A	46.31 ± 0.92	72.89 ± 1.45	102.69 ± 2.04	161.63 ± 3.21	44.524 ± 1.186	44.523 ± 1.149
100816A	18.69 ± 0.42	31.60 ± 0.71	5.82 ± 0.13	9.84 ± 0.22	44.979 ± 1.281	44.899 ± 1.247
091029	2.10 ± 0.07	2.91 ± 0.10	13.76 ± 0.47	19.03 ± 0.64	46.832 ± 1.218	46.970 ± 1.182
091018	13.98 ± 0.33	18.89 ± 0.45	6.96 ± 0.16	9.41 ± 0.22	41.541 ± 1.549	41.698 ± 1.515
090926B	3.10 ± 0.18	5.83 ± 0.33	2.84 ± 0.16	5.34 ± 0.31	45.923 ± 1.190	45.725 ± 1.153
090618	55.98 ± 0.70	79.79 ± 1.00	6.58 ± 0.08	9.37 ± 0.12	43.072 ± 1.190	43.176 ± 1.153
090429B	1.19 ± 0.09	1.90 ± 0.15	140.28 ± 10.69	224.69 ± 17.13	48.601 ± 1.191	48.581 ± 1.155
090424	88.74 ± 1.52	140.49 ± 2.41	10.61 ± 0.18	16.80 ± 0.29	42.200 ± 1.204	42.190 ± 1.167
090423	1.42 ± 0.10	2.17 ± 0.16	115.40 ± 8.28	176.88 ± 12.69	48.410 ± 1.190	48.438 ± 1.153
081222	10.56 ± 0.17	15.28 ± 0.24	70.22 ± 1.11	101.61 ± 1.61	46.446 ± 1.211	46.536 ± 1.175
081221	19.28 ± 0.32	29.27 ± 0.49	78.06 ± 1.31	118.47 ± 1.98	44.406 ± 1.179	44.443 ± 1.142
081121	5.93 ± 0.82	10.24 ± 1.42	31.10 ± 4.31	53.67 ± 7.44	46.832 ± 1.337	46.731 ± 1.305
080916A	3.16 ± 0.14	5.05 ± 0.23	0.67 ± 0.03	1.08 ± 0.05	45.736 ± 1.218	45.714 ± 1.182
080913	1.51 ± 0.13	2.40 ± 0.21	74.69 ± 6.51	118.39 ± 10.31	49.161 ± 1.370	49.153 ± 1.338
080605	38.23 ± 0.70	53.51 ± 0.98	70.16 ± 1.29	98.21 ± 1.81	45.363 ± 1.357	45.490 ± 1.324
080603B	3.73 ± 0.13	5.58 ± 0.19	23.11 ± 0.81	34.56 ± 1.20	46.440 ± 1.202	46.493 ± 1.165
080413B	20.41 ± 0.53	31.71 ± 0.83	13.87 ± 0.36	21.55 ± 0.56	43.642 ± 1.213	43.652 ± 1.176
080207	1.25 ± 0.23	1.85 ± 0.34	4.15 ± 0.76	6.14 ± 1.12	48.056 ± 1.400	48.121 ± 1.370
071010B	8.95 ± 0.21	12.93 ± 0.31	4.19 ± 0.10	6.05 ± 0.14	43.787 ± 1.222	43.875 ± 1.183
070521	11.45 ± 0.29	17.53 ± 0.44	1.43 ± 0.04	2.18 ± 0.06	45.481 ± 1.362	45.510 ± 1.331
070508	50.66 ± 0.78	72.50 ± 1.12	16.59 ± 0.26	23.74 ± 0.37	44.653 ± 1.311	44.755 ± 1.278
060927	2.66 ± 0.10	4.00 ± 0.15	94.65 ± 3.63	142.63 ± 5.48	47.867 ± 1.213	47.914 ± 1.176
060707	0.91 ± 0.13	1.55 ± 0.22	10.12 ± 1.41	17.27 ± 2.40	48.170 ± 1.219	48.080 ± 1.184
060206	2.90 ± 0.11	4.35 ± 0.16	47.87 ± 1.78	71.83 ± 2.67	47.382 ± 1.211	47.433 ± 1.175
060115	0.83 ± 0.07	1.30 ± 0.11	9.85 ± 0.83	15.49 ± 1.30	48.203 ± 1.233	48.201 ± 1.197
050525A	43.25 ± 0.59	74.53 ± 1.02	6.73 ± 0.09	11.59 ± 0.16	42.481 ± 1.201	42.378 ± 1.163

Table 4. The best-fitting parameters of $E_p - E_{\text{iso}}$ relation and $E_p - L$ relation. The errors are of 1σ C.L. The last column gives the Pearson’s linear correlation coefficient.

	σ_{int}	a	b	ρ
$E_p - E_{\text{iso}}$ (CPL)	0.480 ± 0.052	52.764 ± 0.079	1.021 ± 0.258	0.516
$E_p - E_{\text{iso}}$ (Band)	0.462 ± 0.050	52.949 ± 0.076	1.047 ± 0.248	0.541
$E_p - L$ (CPL)	0.463 ± 0.052	52.323 ± 0.078	1.650 ± 0.259	0.691
$E_p - L$ (Band)	0.449 ± 0.050	52.519 ± 0.076	1.652 ± 0.251	0.702

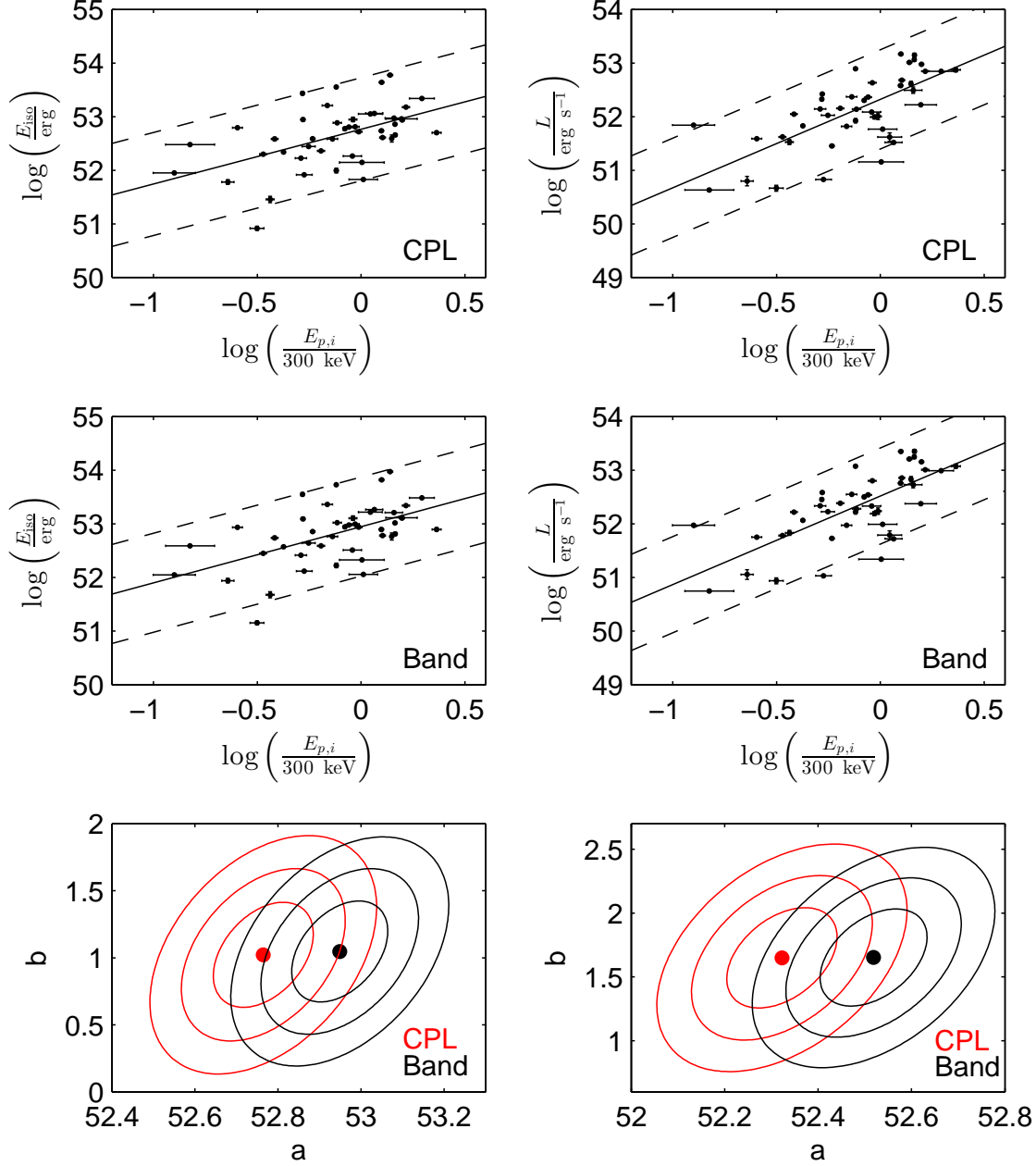


Figure 4. The $E_p - E_{\text{iso}}$ relation (left three panels) and $E_p - L$ relation (right three panels). The solid lines are the best-fitting results, and the dotted lines represent the 2σ scatters. Top two panels: in the case of CPL spectrum. Middle two panels: in the case of Band spectrum. Bottom two panels: the 1σ , 2σ and 3σ contours in the (a, b) plane, red in the CPL case and black in the Band case.

et al. (2007)³. The best-fitting parameters of Yonetoku rela-

³ In the work of Cabrera et al. (2007), the authors parameterized the Amati relation as $\log(E_{p,i}/\text{keV}) = a' + b' \log(E_{\text{iso}}/\text{erg})$. They found that a' in the Band case is smaller than in the CPL cases. A smaller a' corresponds to a larger a in our parametrization.

tion are well consistent with the results of Schaefer (2007). However, the slope parameters of Amati relation are somehow smaller than previous results (Amati et al. 2002; Amati 2003, 2006). One possible reason for the discrepancy may be that our sample is purely obtained from the Swift catalog, while previous works collected sample from other catalog (or

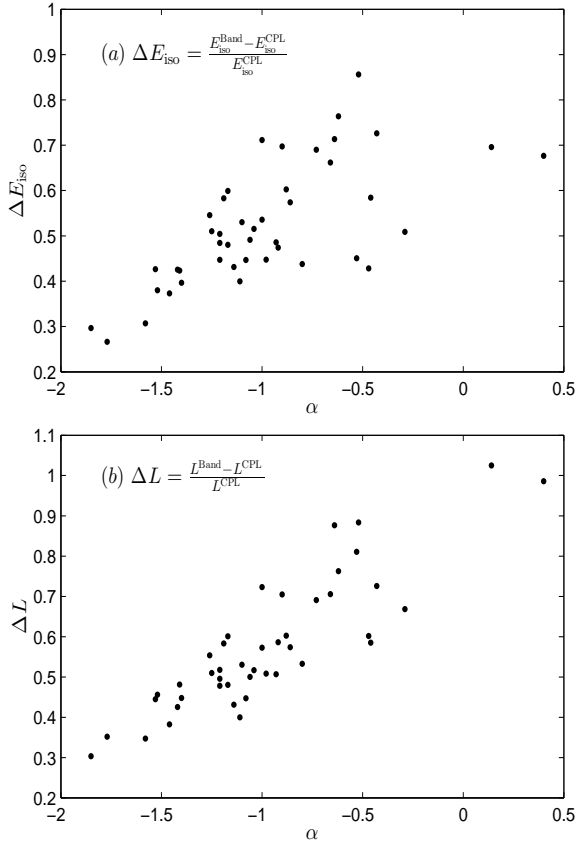


Figure 3. Top panel: the correlation between ΔE_{iso} and α . Bottom panel: the correlation between ΔL and α .

the combination of various catalogs). For example, Amati (2006) calculated the $E_p - E_{\text{iso}}$ relation of 41 GRBs from the combination of BATSE, BeppoSAX, HETE-2, Konus and Swift catalogs, and found a slope of ~ 2 . In the $E_p - E_{\text{iso}}$ plot, the Swift subsample seems to fall near the best-fitting line of the full sample. Therefore, he claimed that the Swift subsample follows the same $E_p - E_{\text{iso}}$ relation of the full sample. However, Amati (2006) has not calculated the slope parameter for the Swift subsample alone. In fact, if we only consider the 9 Swift GRBs corrected in table 1 of Amati’s paper, we get a slope of ~ 1.26 , which is much flatter than that of the full sample. For the pure Swift GRBs collected in Table 13 of Sakamoto et al. (2011), we get a slope of ~ 1.47 , still much smaller than the originally proposed value ~ 2 (Amati et al. 2002). This may imply that the Swift GRBs have a flatter $E_p - E_{\text{iso}}$ slope than other GRBs. In the bottom two panels of Figure 4, we plot the 1σ , 2σ and 3σ contours in the (a, b) plane. Red contours represent the CPL case and black contours represent the Band case. The best-fitting values are denoted by dots. It seems that both $E_p - E_{\text{iso}}$ relation and $E_p - L$ relation in the Band cases are differs from that in the CPL case at about 2σ C.L. In the last column of Table 4, we also list the Pearson’s linear correlation coefficient. We can see that the correlations in the CPL case are as tight as that in the Band case. However, both correlations are not as tight as previously claimed. The intrinsic scatters of

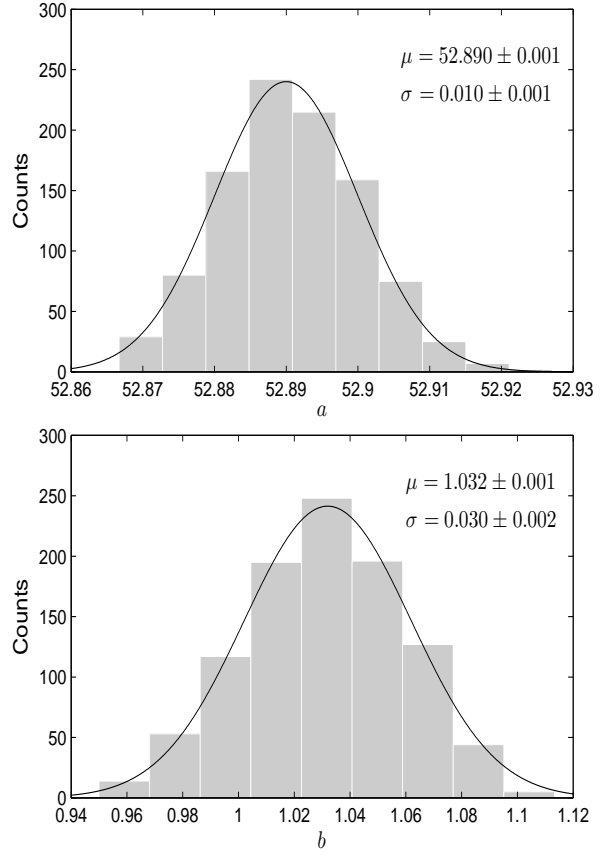


Figure 5. The histograms of a and b in 1000 simulations. The solid curves are the best-fitting results to Gauss function.

both luminosity correlations are comparable to the results of Wang, Qi & Dai (2011).

Among the 44 Swift-BAT GRBs considered here, at least 24 of them are also observed by Konus-Wind (Aptekar et al. 1995) or Fermi-GBM (Meegan et al. 2009). These two detectors can observe GRBs in a much wider energy band (10 keV – 10 MeV for Konus-Wind and 8 keV – 40 MeV for Fermi-GBM) than Swift-BAT, making the detailed analysis of spectra possible. We list the spectral properties of these 24 GRBs in Table 5. The spectra of 10 GRBs can be fitted to the Band function, so that the high-energy index β can be well constrained. For the remain 14 GRBs, the spectra can only be fitted to CPL, and β still can’t be constrained. In column (8) of Table 5, we also list the isotropic-equivalent energy E_{iso} . For GRBs which have well measured β , E_{iso} is calculated from the Band model. Otherwise, E_{iso} is calculated from the CPL model. With these 24 GRBs, we calculate the Amati relation and obtain parameters $a = 52.749 \pm 0.143$, $b = 1.285 \pm 0.538$, $\sigma_{\text{int}} = 0.701 \pm 0.101$. Due to the narrow coverage of E_p and the small sample, the intrinsic scatter is large and the slope parameter couldn’t be well constrained. Nevertheless, the slope still seems to be flatter than previous findings, but consistent with our results. It is not clearly understood why Swift GRBs have flatter slope. One reason may be that the peak energies measured by Swift/BAT have a relatively narrow distribution (e.g., most of $E_{p,i}$ ’s are between 50 and

Table 5. The properties of Swift-BAT GRBs observed by Konus-Wind or Fermi-GBM. Column (1): the GRB identifier. Column (2): the redshift. Column (3): the observed photon fluence in unit of 10^{-7} erg cm $^{-2}$. Column (4): the low-energy photon index. Column (5): the high-energy photon index. Column (6): the observed peak energy in unit of keV. Column (7): the energy band in which the photon fluence is calculated, in unit of keV. Column (8): the isotropic equivalent energy in unit of 10^{52} ergs. Column (9): the detector by which the GRB was observed, KON for Konus-Wind and GBM for Fermi-GBM. Column (10): the GCN Circular numbers. All the errors in this table are of 90% C.L.

(1) GRBs	(2) z	(3) S	(4) α	(5) β	(6) E_p	(7) $E_{\min} - E_{\max}$	(8) E_{iso}	(9) Detector	(10) GCN Circ
141220A	1.3195	$52.3^{+1.5}_{-1.5}$	$-0.80^{+0.05}_{-0.05}$...	180^{+9}_{-9}	8 – 1000	$2.48^{+0.07}_{-0.07}$	GBM	17205
140206A	2.73	147^{+3}_{-3}	$-0.20^{+0.10}_{-0.10}$	$-2.40^{+0.10}_{-0.10}$	120^{+6}_{-6}	10 – 1000	$29.14^{+0.59}_{-0.59}$	GBM	15796
130925A	0.347	$2.83^{+0.06}_{-0.06}$	$-1.50^{+0.05}_{-0.05}$...	107^{+3}_{-3}	10 – 1000	$0.01^{+0.01}_{-0.01}$	GBM	15261
130701A	1.155	58^{+2}_{-2}	$-1.10^{+0.10}_{-0.10}$...	89^{+4}_{-4}	20 – 1200	$2.64^{+0.09}_{-0.09}$	KON	14958
120922A	3.1	65^{+4}_{-4}	$-1.60^{+0.70}_{-0.70}$	$-2.30^{+0.10}_{-0.10}$	$37.7^{+3.5}_{-3.5}$	10 – 1000	$21.59^{+1.33}_{-1.33}$	GBM	13809
120326A	1.798	$35.39^{+1.74}_{-1.74}$	$-0.98^{+0.14}_{-0.14}$	$-2.53^{+0.15}_{-0.15}$	$46.5^{+3.7}_{-3.7}$	10 – 1000	$3.62^{+0.18}_{-0.18}$	GBM	13145
110715A	0.82	230^{+20}_{-20}	$-1.23^{+0.09}_{-0.09}$	$-2.70^{+0.20}_{-0.20}$	120^{+12}_{-12}	20 – 10000	$4.92^{+0.43}_{-0.43}$	KON	12166
110422A	1.77	856^{+2}_{-2}	$-0.65^{+0.06}_{-0.06}$	$-2.96^{+0.14}_{-0.14}$	152^{+5}_{-5}	20 – 2000	$74.59^{+0.17}_{-0.17}$	KON	11971
100816A	0.8034	33^{+4}_{-4}	$-1.00^{+0.40}_{-0.30}$...	148^{+41}_{-26}	20 – 2000	$0.65^{+0.08}_{-0.08}$	KON	11127
090926B	1.24	87^{+3}_{-3}	$-0.13^{+0.06}_{-0.06}$...	91^{+2}_{-2}	10 – 1000	$3.65^{+0.13}_{-0.13}$	GBM	9957
090618	0.54	2700^{+60}_{-60}	$-1.26^{+0.06}_{-0.02}$	$-2.50^{+0.15}_{-0.33}$	$155.5^{+11.1}_{-10.5}$	8 – 1000	$25.87^{+0.57}_{-0.57}$	GBM	9535
090424	0.544	520^{+10}_{-10}	$-0.90^{+0.02}_{-0.02}$	$-2.90^{+0.10}_{-0.10}$	177^{+3}_{-3}	8 – 1000	$4.55^{+0.09}_{-0.09}$	GBM	9230
090423	8	11^{+3}_{-3}	$-0.77^{+0.35}_{-0.35}$...	82^{+15}_{-15}	8 – 1000	$10.61^{+2.89}_{-2.89}$	GBM	9229
081222	2.77	132^{+48}_{-40}	$-0.67^{+0.39}_{-0.33}$	$-2.35^{+0.30}_{-1.25}$	165^{+47}_{-29}	20 – 1000	$28.67^{+10.43}_{-8.69}$	KON	8721
081221	2.26	228^{+7}_{-7}	$-0.91^{+0.15}_{-0.14}$...	83^{+4}_{-4}	20 – 1000	$35.11^{+1.08}_{-1.08}$	KON	8694
081121	2.512	179^{+37}_{-31}	$-0.77^{+0.15}_{-0.14}$	$-2.51^{+0.31}_{-0.66}$	248^{+38}_{-33}	20 – 7000	$25.78^{+5.33}_{-4.46}$	KON	8548
080916A	0.689	$55.4^{+7.9}_{-6.6}$	$-1.00^{+0.38}_{-0.32}$...	129^{+33}_{-21}	20 – 1000	$0.81^{+0.12}_{-0.10}$	KON	8259
080913	6.44	$8.5^{+6.0}_{-2.2}$	$-0.89^{+0.65}_{-0.46}$...	131^{+225}_{-48}	15 – 1000	$6.20^{+4.37}_{-1.60}$	KON	8256
080605	1.6398	302^{+13}_{-12}	$-1.03^{+0.07}_{-0.07}$...	252^{+20}_{-17}	20 – 2000	$22.82^{+0.98}_{-0.91}$	KON	7854
080603B	2.69	$45.0^{+15.3}_{-9.0}$	$-1.23^{+0.75}_{-0.54}$...	102^{+119}_{-28}	20 – 1000	$9.81^{+3.33}_{-1.96}$	KON	7812
071010B	0.947	$47.8^{+9.5}_{-31.2}$	$-1.25^{+0.74}_{-0.49}$	$-2.65^{+0.29}_{-0.49}$	52^{+10}_{-14}	20 – 1000	$1.76^{+0.35}_{-1.15}$	KON	6879
070521	0.553	181^{+6}_{-31}	$-0.93^{+0.12}_{-0.12}$...	222^{+27}_{-21}	20 – 1000	$1.58^{+0.05}_{-0.27}$	KON	6459
070508	0.82	397^{+7}_{-23}	$-0.81^{+0.07}_{-0.07}$...	188^{+8}_{-8}	20 – 1000	$7.72^{+0.14}_{-0.45}$	KON	6403
050525A	0.606	784^{+6}_{-6}	$-1.10^{+0.05}_{-0.05}$...	$84.1^{+1.7}_{-1.7}$	20 – 1000	$9.81^{+0.08}_{-0.08}$	KON	3474

500 keV), while the samples investigated previously cover at least 3 orders of magnitude in $E_{p,i}$ (from a few keV to a few thousands keV).

To test the sensitivity of luminosity correlations on the high-energy power-law index β , we implement the Monte Carlo simulations. We recalculate the Amati relation in the case that GRB spectra are modeled by the Band function. In this time, β is no longer fixed at -2.2 , but it is a random number generated from the Gauss distribution with average value -2.2 and standard deviation 0.4^4 . We simulate 1000 times and derive the intercept and slope parameters (a, b) of Amati relation in each simulation. The histograms of a and b in 1000 simulations are plotted in Figure 5. The distribution of both a and b can be well fitted by Gauss function, with average values and standard deviations $\mu_a = 52.890 \pm 0.001$, $\sigma_a = 0.010 \pm 0.001$ (95% C.L.), and $\mu_b = 1.032 \pm 0.010$, $\sigma_b = 0.030 \pm 0.002$ (95% C.L.), respectively. This is consistent with the Amati relation in both the CPL and Band cases (see Table 4). The small standard deviations of a and b imply that the Amati relation is insensitive to β . Since the Yonetoku relation in the CPL cases does not much differ

from that in the Band case, we can expect that it is also insensitive to β .

4 DISTANCE CALIBRATION AND GRB HUBBLE DIAGRAM

Both the Amati relation and Yonetoku relation have been widely used to calibrate the distance of GRBs. Here we take the Amati relation as an example. The calibrating procedures are as follows: first, derive the best-fitting parameters (a, b) of Amati relation as discussed in the last section. Second, calculate E_{iso} of each GRB through Eq.(4), by fixing (a, b) at the best-fitting values. Then the luminosity distance of each GRB can be obtained through Eq.(5). Finally, convert the luminosity distance to distance modulus, i.e.,

$$\mu(z) = 5 \log \frac{d_L(z)}{\text{Mpc}} + 25. \quad (14)$$

The uncertainty of distance modulus is calculated using the formulae of error propagation (Schaefer 2007),

$$\sigma_\mu^2 = \left(\frac{5}{2 \ln 10} \right)^2 \left[(\ln 10)^2 \sigma_{\log E_{\text{iso}}}^2 + \frac{\sigma_{S_{\text{bolo}}}^2}{S_{\text{bolo}}^2} \right], \quad (15)$$

⁴ We constrain β to be smaller than -2 , such that E_p is well defined. This can be done by setting β to its symmetrical value for any $\beta \geq -2$, i.e., using $\beta' = -4.4 - \beta$ instead of β . The price is that the distribution of β is not strictly Gaussian.

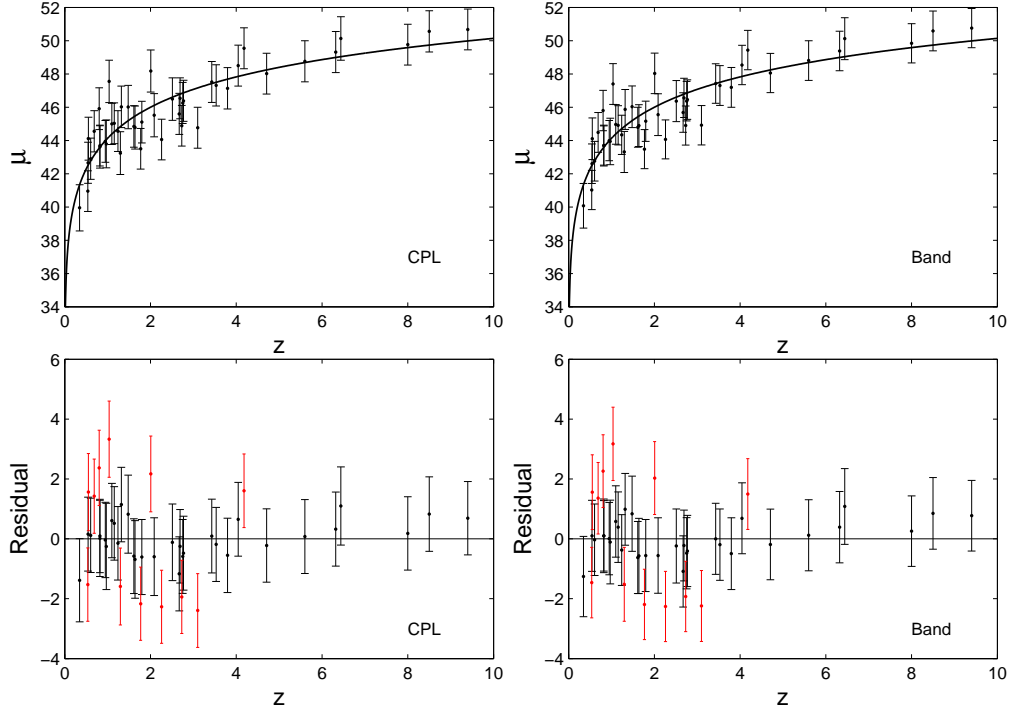


Figure 6. The GRB Hubble diagram and residuals of distance moduli, calibrated using the Amati relation. Left two panels: in the case of CPL spectrum. Right two panels: in the case of Band spectrum. In the top two panels, the black curve is the theoretical result of concordance Λ CDM model ($\Omega_M = 0.28$, $\Omega_\Lambda = 0.72$, $H_0 = 70 \text{ km s}^{-1} \text{ Mpc}^{-1}$). In the bottom two panels, the black (red) error bars represent that the calibrated distance moduli are consistent (inconsistent) with the Λ CDM model within 1σ uncertainty.

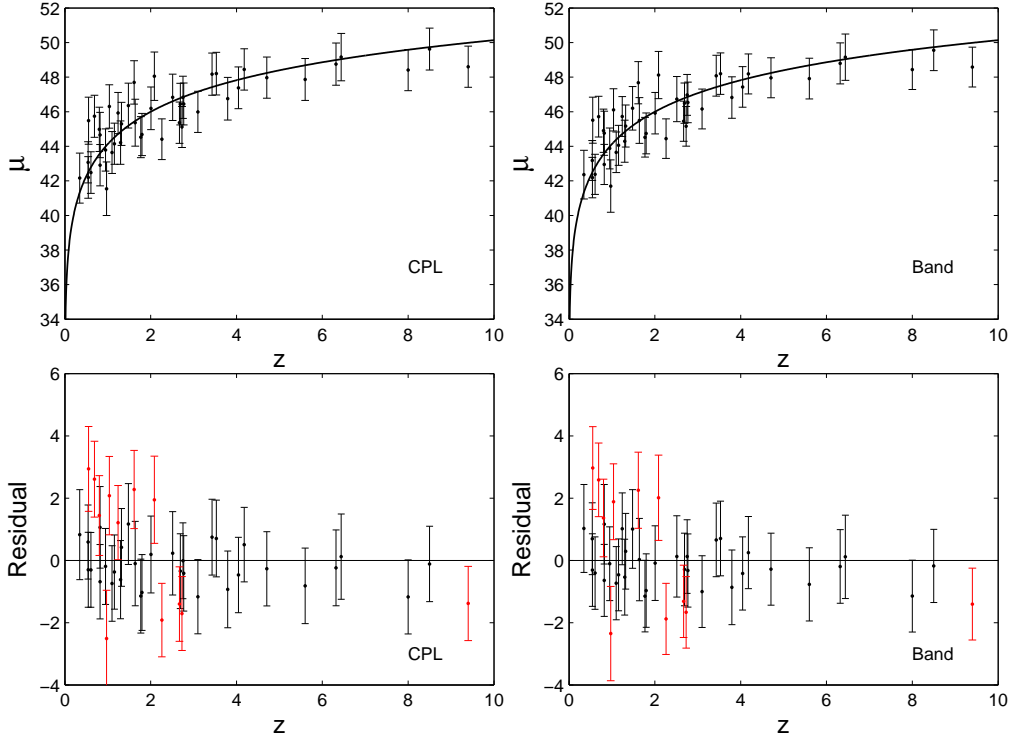


Figure 7. The same to Figure 6, except that the distance moduli are calibrated using the Yonetoku relation.

where

$$\sigma_{\log E_{\text{iso}}}^2 = \sigma_a^2 + \left(\sigma_b \log \frac{E_{p,i}}{300 \text{ keV}} \right)^2 + \left(\frac{b}{\ln 10} \frac{\sigma_{E_{p,i}}}{E_{p,i}} \right)^2 + \sigma_{\text{int}}^2. \quad (16)$$

We can also calibrate GRBs using the Yonetoku relation in a very similar way.

We must point out that the calibrating method mentioned above has the circularity problem and is model dependent, because we have used the concordance cosmological model with fiducial parameters in the calibration. Our paper is not aimed at solving this problem, but we are rather interested in studying the effect of GRB spectra on the distance calibration. Some model-independent methods free of circularity problem have been extensively discussed (Liang et al. 2008; Liang & Zhang 2008; Wei & Zhang 2009; Wei 2010; Liu & Wei 2014).

The distance moduli calibrated using the Amati relation and Yonetoku relation are listed in columns (6) – (7) in Table 2 and Table 3, respectively. We can see that the distance moduli only slightly depend on the choice of GRB spectra. The difference between distance moduli in the two spectra cases (Band and CPL) is much smaller than the uncertainties of distance moduli, i.e., $|\mu^{\text{Band}} - \mu^{\text{CPL}}| \ll \sigma_\mu$. In Figure 6, we plot the GRB Hubble diagram calibrated using Amati relation. The top-left and top-right panels are the resulting Hubble diagram in the CPL and Band cases, respectively. The solid curves are the theoretical results of concordance Λ CDM model with fiducial parameters $H_0 = 70 \text{ km s}^{-1} \text{ Mpc}^{-1}$, $\Omega_M = 0.28$ and $\Omega_\Lambda = 0.72$. In the bottom two panels of Figure 6, we plot the residual of distance moduli with respect to the theoretical curve. The error bar represents 1σ uncertainty. GRBs consistent (inconsistent) with theoretical curve within 1σ uncertainty are denoted by black (red). Due to the large intrinsic scatter of Amati relation, 27% (12 out of 44) GRBs do not fall onto the theoretical curve within 1σ uncertainty. These GRBs all have low redshift ($z \lesssim 4$). GRBs inconsistent with theoretical curve in the CPL case are still inconsistent in the Band case. The uncertainty of distance modulus mainly ($\gtrsim 90\%$) propagates from the intrinsic scatter. A much tighter correlation with smaller intrinsic scatter is necessary to reduce σ_μ .

We also reconstruct the GRB Hubble diagram using the Yonetoku relation and plot it in Figure 7. Compared to the Hubble diagram reconstructed from Amati relation, very similar conclusion can be draw. Therefore, we conclude that the GRB Hubble diagram almost does not depend on the choice of GRB spectra.

5 SUMMARY

In this paper, we have investigated the effect of GRB spectra on the luminosity correlations and GRB Hubble diagram. Most previous works calculated the isotropic equivalent energy and peak luminosity by assuming that GRB spectra are modeled by the Band function. Due to the narrow energy coverage of detectors, the high-energy power-law index of Band function usually can't be constrained. Using 44 Swift GRBs with well determined peak energy, we calculated two luminosity correlations (Amati relation and Yonetoku relation) in the cases that GRB spectra are modeled

by the Band function and CPL, respectively. It is found that both Amati relation and Yonetoku relation only moderately depend on the choice of GRB spectra. Monte Carlo simulations show that the Amati relation is insensitive to the high-energy power-law index of Band function. We further calibrated the distance of GRBs using these two luminosity correlations and reconstructed the GRB Hubble diagram. We found that different GRB spectra only cause the difference of distance modulus at the order of 0.1 mag, while the uncertainty of distance modulus calibrated using luminosity correlations are usually larger than 1.0 mag. Therefore, we may conclude that the resulting GRB Hubble diagram is insensitive to the choice of GRB spectra.

ACKNOWLEDGEMENTS

We are grateful to J. Li, H. Ma and L. Tang for useful discussions. X. Li has been supported by the National Natural Science Fund of China (NSFC) (Grant No. 11305181 and 11547305) and the Open Project Program of State Key Laboratory of Theoretical Physics, Institute of Theoretical Physics, Chinese Academy of Sciences, China (No. Y5KF181CJ1). Z. Chang has been funded by the NSFC under Grant No. 11375203.

References

- Amati L., et al., 2002, *A&A*, 390, 81
- Amati L., et al., 2008, *MNRAS*, 391, 577
- Amati L., 2003, *Chin. J. Astron. Astrophys. Supp.*, 3, 455
- Amati L., 2006, *MNRAS*, 372, 233
- Amati L., 2010, *arXiv:1002.2232*
- Amati L., Frontera F., Guidorzi C., 2009, *Astron. Astrophys.*, 508, 173
- Aptekar R. L., et al., 1995, *Space Sci. Rev.*, 71, 265
- Band D., et al., 1993, *ApJ*, 413, 281
- Basilakos S., Perivolaropoulos L., 2008, *MNRAS*, 391, 411
- Bernardini M. G., Margutti R., Zaninoni E., Chincarini G., 2012, *MNRAS*, 425, 1199
- Cabrera J. I., et al., 2007, *MNRAS*, 382, 342
- Cucchiara A., et al., 2011, *ApJ*, 736, 7
- Dai Z. G., Liang E. W., Xu D., 2004, *Astrophys. J.*, 612, L101
- Dainotti M. G., Cardone V. F., Piedipalumbo E., Capozziello S., 2013, *MNRAS*, 436, 82
- D'Agostini G., 2005, *arXiv:physics/0511182* [physics.data-an]
- Fenimore E. E., Ramirez-Ruiz E., 2000, *arXiv: astro-ph/0004176*
- Firmani C., Ghisellini G., Ghirlanda G., Avila-Reese V., 2005, *MNRAS*, 360, L1
- Firmani C., Ghisellini G., Avila-Reese V., Ghirlanda G., 2006, *MNRAS*, 370, 185
- Fishman G., Meegan C., 1995, *Annu. Rev. Astron. Astrophys.*, 33, 415
- Ghirlanda G., Ghisellini G., Lazzati D., 2004, *ApJ*, 616, 331
- Ghirlanda G., Ghisellini G., Lazzati D., Firmani C., 2004, *ApJ*, 613, L13
- Kouveliotou C., et al., 1993, *ApJ*, 413, L101

- Kumar P., Zhang B., 2015, *Phys. Rep.*, 561, 1
- Li L. X., 2007, *MNRAS*, 379, L55
- Liang E. W., Lin T. T., LV J., Lu R., Zhang J., Zhang B., 2015, arXiv:1505.03660
- Liang N., Xiao W. K., Liu Y., Zhang S. N., 2008, *ApJ*, 685, 354
- Liang E. W., Zhang B., 2005, *ApJ*, 633, 611
- Liang N., Zhang S. N., 2008, *AIP Conf. Proc.*, 1065, 367
- Lin H.-N., Li X., Wang S., Chang Z., 2015, *MNRAS*, 453, 128
- Lin H.-N., Li X., Chang Z., 2015, arXiv:1507.06662, accepted by *MNRAS*
- Liu J., Wei H., 2014, arXiv:1410.3960
- Margutti R., et al., 2013, *MNRAS*, 428, 729
- Meegan C. A., Lichti G., Bhat P. N., et al., 2009, *ApJ*, 702, 791
- Mészáros P., 2006, *Rep. Prog. Phys.*, 69, 2259
- Norris J. P., Marani G. F., Bonnell J. T., 2000, *ApJ*, 534, 248
- Paciesas W. S., et al., 1999, *ApJ*, 122, S465
- Piran T., 1999, *Phys. Rep.*, 314, 575
- Preece R. D., et al., 2000, *ApJ*, 126, S19
- Sakamoto T., et al., 2011, *ApJ*, 195, S2
- Schaefer B. E., 2003, *ApJ*, 583, L67
- Schaefer B. E., 2007, *ApJ*, 660, 16
- Wang F. Y., Qi S., Dai Z. G., 2011, *MNRAS*, 415, 3423
- Wang J. S., Wang F. Y., Cheng K. S., Dai Z. G., 2015, arXiv:1509.08558
- Wei H., Zhang S. N., 2009, *Eur. Phys. J. C*, 63, 139
- Wei H., 2010, *J. Cosmol. Astropart. Phys.*, 08, 020
- Xiao L. M., B. E. Schaefer, 2009, *ApJ*, 707, 387
- Yonetoku D., Murakami T., Nakamura T., Yamazaki R., Inoue A. K., Ioka K., 2004, *ApJ*, 609, 935